Applied Catalysis B: Environmental 328 (2023) 122484

Contents lists available at ScienceDirect

Applied Catalysis B: Environmental

journal homepage: www.elsevier.com/locate/apcatb

Coupling oxygen vacancy and hetero-phase junction for boosting catalytic activity of Pd toward hydrogen generation

Ruofan Shen [a], Yanyan Liu [a,b,c,*], Huanhuan Zhang [a], Shuling Liu [a], Huijuan Wei [a], Huiyu Yuan [a], Hao Wen [a], Xianli Wu [a], Sehrish Mehdi [a], Tao Liu [d], Jianchun Jiang [c], Erjun Liang [a,**], Baojun Li [a,e,*]

[a] School of Physics and Microelectronics, College of Chemistry, Zhengzhou University, 100 Science Road, Zhengzhou 450001, PR China
[b] College of Science, Henan Agricultural University, Zhengzhou, Henan 450002, PR China
[c] National Engineering Lab. for Biomass Chemical Utilization, Institute of Chemical Industry of Forest Products, Chinese Academy of Forestry, Nanjing 210042, PR China
[d] CAS Key Laboratory for Biomedical Effects of Nanomaterials and Nanosafety, National Centre for Nanoscience and Technology, Beijing 100190, PR China
[e] Department of Chemistry, Tsinghua University, Beijing 100084, PR China

ARTICLE INFO

Keywords:
Ammonia borane
Hetero-phase junction
Oxygen vacancy
Palladium
Water dissociation

ABSTRACT

Water dissociation is the rate-limiting step of many chemical reactions due to the high activation energy in the step of breaking O-H bond. Herein, an effective approach via coupling oxygen vacancy (V_O) and hetero-phase junction to boost the ability of Pd catalysts toward water dissociation is determined. The Pd catalyst exhibits an outstanding catalytic activity in the hydrolysis of ammonia borane (AB) under alkaline additive-free condition at 298 K with a turnover frequency of 210 min^{-1}. Theoretical simulation and characterization analyses reveal that both the appropriate interfacial charge states benefitting for adsorption caused by hetero-phase junction and the electron-rich Pd caused by V_O enhance the intrinsic catalytic activity of Pd toward water dissociation in AB hydrolysis. This proof-of-concept research provides a valuable strategy for catalyst design, via coupling V_O and hetero-phase junction to improve the reaction kinetics by boosting water dissociation in the field of catalytic energy conversion.

1. Introduction

The development of renewable energy sources has become an indispensable strategy to solve the energy shortage and environmental pollution in modern society [1–4]. Hydrogen production from chemical hydrogen storage materials is beneficial to the further application of hydrogen energy by virtue of its advantages such as convenience, low cost, high efficiency and strong practicability [5,6]. Ammonia borane (NH_3BH_3, AB) is expected to be a promising hydrogen storage material for small energy installations due to its high content of hydrogen element (19.6 *wt.* %), pollution-free and high stability at room temperature [7–10]. Nevertheless, the application of AB hydrolysis is limited by sluggish kinetics because of the high activation energy for water dissociation, the rate-limiting step (RLS) in overall reaction (Eqs. 1–3, α* and β* stand for active sites) [11,12]. Thus, design of highly active catalysts for water dissociation is the key to efficient hydrogen evolution from AB hydrolysis.

$$H_2O+2\alpha^* \rightarrow \alpha\text{-}H^*+\alpha\text{-}OH^* \quad (1)$$

$$NH_3BH_3+2\beta^* \rightarrow \beta\text{-}NH_3BH_2^*+\beta\text{-}H^* \quad (2)$$

$$\alpha\text{-}H^*+\beta\text{-}H^* \rightarrow H_2+\alpha^*+\beta^* \quad (3)$$

In existing studies, transition metals are often used as the active sites of catalysts for AB hydrolysis [13,14]. Fe, Co, Ni, Cu and corresponding oxides are often used as supports or active sites of catalysts. At present, construction of lamellar and core-shell structured catalysts, synergistic effects among metal active sites and surface phosphating of metal active sites are commonly used in improving the activity of non-noble metal-based catalysts for AB hydrolysis [15–18]. Due to the intrinsic properties of non-noble metals, there are some problems such as low catalytic activity, fast deactivation of catalyst, complex catalytic components and limit mechanism interpretation in the development of industrial

* Corresponding authors at: School of Physics and Microelectronics, College of Chemistry, Zhengzhou University, 100 Science Road, Zhengzhou 450001, PR China.
** Corresponding author.
E-mail addresses: lyylhs180208@163.com (Y. Liu), ejliang@zzu.edu.cn (E. Liang), lbjfcl@zzu.edu.cn (B. Li).

https://doi.org/10.1016/j.apcatb.2023.122484
Received 3 January 2023; Received in revised form 14 February 2023; Accepted 16 February 2023
Available online 17 February 2023

catalysts for hydrogen production from AB [19,20]. The catalytic activity of non-noble metal-based catalysts is much lower than that of noble metal-based catalysts [21,22]. Compared with the counterparts of those noble metals, the low stability induced by severe aggregation of non-noble metal nanoparticles (NPs) make problems for non-noble metal-based catalysts to maintain high activity during actual reaction processes [23]. Therefore, highly active and robust catalysts with adjustable surface electronic properties can be obtained via modifying or coupling noble metals to non-noble metal oxides due to the abundant tunable valence states of non-noble metals.

Pd was initially used in the catalysts design for AB hydrolysis because of lower price and higher stability than other noble metals. Moderate catalytic activities are obtained in AB hydrolysis with turnover frequency (*TOF*) of 29.0 min^{-1} on Pd^0/CeO_2 catalyst and 7.1 min^{-1} on Pd^0/nano TiO_2 catalyst [24]. Compared with Pd^0/nano TiO_2, the higher *TOF* on Pd^0/CeO_2 is improved by the strong interaction between Pd and negative charges on the defective surface of CeO_2. High activity in AB dissociation and low activity in water dissociation induced by excess negative charges results in low overall activity in AB hydrolysis. However, the intrinsic activity of Pd toward water dissociation is limited by the electronic properties of Pd. The activity of pristine Pd-based catalysts in AB hydrolysis requires for an effective promotion [25]. The construction of electronic states of Pd active sites conducive to the desorption and dissociation of water molecules are the key to the rational design of Pd-based catalysts with higher activity.

Constructing a hetero-phase junction in catalysts is an effective method to promote the water dissociation [26–29]. The electronic properties of different components in hetero-phase junction induce to some appropriate interfacial charge states for the sorption of reactant molecules and the improvement of the catalytic activity [29]. As a typical defect in oxides, oxygen vacancy (V_O) shows some promising capability to boost the intrinsic activity toward water dissociation in photo- and electro-catalysis [30–36]. The introduction of V_O into catalysts facilitates the electron aggregation at V_O and the electron transfer between support and metal to generate abundant highly active sites for water dissociation [3,8,35]. As an imaginary atom, V_O promotes the catalytic hydrolysis of AB on TiO_2-V_O-Ru at room temperature through the electron promoter effect [35]. TiO_2 (P25) is a favorite subject to research the effect of hetero-phase junction on catalytic property because of unique phase composition, high chemical stability, pollution-free and low cost [37]. These valuable works provide a meaningful guidance for coupling V_O and hetero-phase junction to efficiently activate water molecules. Up to date, the construction of novel catalysts with precise structure and corresponding catalytic mechanism based on coupling V_O and hetero-phase junction is aspired to be explored in the field of hydrogen generation.

In this work, an effective approach via coupling V_O and hetero-phase junction to improve the ability of catalyst to dissociate water molecules is demonstrated. Theoretical simulation and characterization analyses reveal that both the appropriate interfacial charge states benefitting for adsorption caused by hetero-phase junction and the electron-rich Pd caused by V_O enhance the intrinsic catalytic activity of Pd toward water dissociation. Outstanding *TOF* (210 min^{-1} calculated based on the overall Pd content, 981 min^{-1} calculated based on Pd dispersion) is achieved on the optimized $PdCoO_xP25$ catalyst in AB hydrolysis. The activity of $PdCoO_xP25$ precedes all current reported catalysts composed of TiO_2 and Pd NPs. In the reaction between AB and methanol (CH_3OH), the coupling of V_O and hetero-phase junction still contribute. This research confirms the potential of coupling V_O and hetero-phase junction in the field of catalytic conversion of energy sources.

2. Experimental section

Preparation of catalysts. In the experiment, Pd was supported on rutile TiO_2 (TR), anatase TiO_2 (TA) and P25, and denoted as PdTR, PdTA and PdP25, respectively. Palladium(II) acetylacetonate ($Pd(acac)_2$) (13.2 mg) was thoroughly mixed with TR (300 mg), TA (300 mg) and P25 (300 mg), respectively, and then incubated at 250 °C in argon for 60 min. $Pd(acac)_2$ was reduced to elemental Pd by self-carbon source. Then PdP25 was selected for further experiment because of its highest catalytic activity.

P25 (300 mg) and $Pd(acac)_2$ (13.2 mg) were thoroughly mixed with Iron(III) 2,4-pentanedionate ($Fe(C_5H_7O_2)_3$, $Fe(acac)_3$) (15.6 mg), Copper(III) acetylacetonate ($Co(acac)_2$) (11.4 mg), Nickel(II) acetylacetonate ($Ni(acac)_2{\cdot}2H_2O$) (12.9 mg) and Cupric(II) acetylacetonate ($Cu(acac)_2$) (11.6 mg), respectively. The ratio of non-noble metals to Pd is optimized, and the amount of Fe, Co, Ni or Cu in the catalyst was equal to the amount of Pd. The non-noble metal salts were reduced to metal oxides by their own carbon source under 250 °C in argon, and the holding time was 60 min. The catalysts were denoted as $PdFeO_xP25$, $PdCoO_xP25$, $PdNiO_xP25$ and $PdCuO_xP25$, respectively. $PdAl_2O_3$, $PdSiO_2$, $PdCoO_xAl_2O_3$, $PdCoO_xSiO_2$, $PdCoO_xTA$ and $PdCoO_xTR$ were also prepared under the same conditions. CoO_x modified PdP25 were obtained by different treating time. $PdCoO_x$ was also prepared under the same conditions. All samples were stored in a vacuum package.

Hydrogen generation methods. A magneton and catalyst (10 mg) were added into a flask on a magnetic stirrer. The stirring speed was fixed at 1000 rpm. AB (44 mg) and H_2O (5 mL) or CH_3OH (5 mL) were injected into the flask. Hydrogen was collected in a cylinder by drainage.

Characterization. The catalyst structure information was obtained from the following tests. X-ray powder diffraction (XRD), transmission electron microscope (TEM), high angle annular dark field scanning transmission electron microscope (HAADF-STEM), energy dispersive X-ray (EDX), electron paramagnetic resonance (EPR) spectra, UV-Vis diffuse reflectance spectra, X-ray photoelectron spectrum (XPS), quantachrome autosorb-IQ gas adsorption analyzer, inductively coupled plasma-optical emission spectroscopy (ICP-OES), Raman spectra, Xray absorption spectroscopy (XAFS), density functional theory (DFT) simulation.

Additionally, the detailed characterization of the activity and structure of catalysts are given in Supporting Information.

3. Results and discussion

3.1. Catalytic performances

The activity of the fresh and recycled catalysts in AB hydrolysis were tested under alkaline additive-free condition, avoiding the generation of ammonia. The *TOF* on $PdCoO_x$, $PdTiO_2$-rutile (PdTR), $PdTiO_2$-anatase (PdTA) and PdP25 at 298 K are 0, 10, 63 and 114 min^{-1}, respectively (Fig. S2a and Fig. 1a-b) [38]. The hetero-phase junction in P25 is beneficial to the pre-adsorption of AB and water molecules, resulting in a higher catalytic activity of PdP25 [39,40]. The ratio of non-noble metals to Pd has been optimized (Fig. S2c and d). The *TOF* on PdP25, $PdCuO_xP25$, $PdFeO_xP25$, $PdNiO_xP25$, $PdCoO_xP25$ and CoO_xP25 at 298 K are 114, 128, 133, 154, 210 and 0 min^{-1}, respectively (Fig. 1c, Fig. 1d and Table S1). The highest *TOF* on $PdCoO_xP25$ suggests the highest catalytic activity. In the pyrolysis process of $Co(acac)_2$ in argon, incomplete oxidation of Co is caused by the lack of oxygen. The effect of CoO_x obtained at different reduction times (20 min, 40 min and 60 min) on the activity of $PdCoO_xP25$ is investigated (Fig. 1e and f). Further analysis confirmed a positive correlation between catalyst activity and V_O concentration. The detailed analysis is given in the discussion below. CoO_x without V_O and hydrogen production data with comparative value could not be obtained by the same method (Figs. S1 and S2a-b). Therefore, different vectors were used in this experiment to verify the contribution of CoO_x. The *TOF* on $PdCoO_xAl_2O_3$, $PdCoO_xSiO_2$, $PdCoO_xTA$ and $PdCoO_xTR$ is higher than that of $PdAl_2O_3$, $PdSiO_2$, PdTA and PdTR (Fig. S3a and b). The introduction of CoO_x further improves the activity of Pd catalyst toward AB hydrolysis. Since the reaction process is carried out under magnetic agitation, the effect of magnetic component in supports are not considered independently [41]. The *TOF*

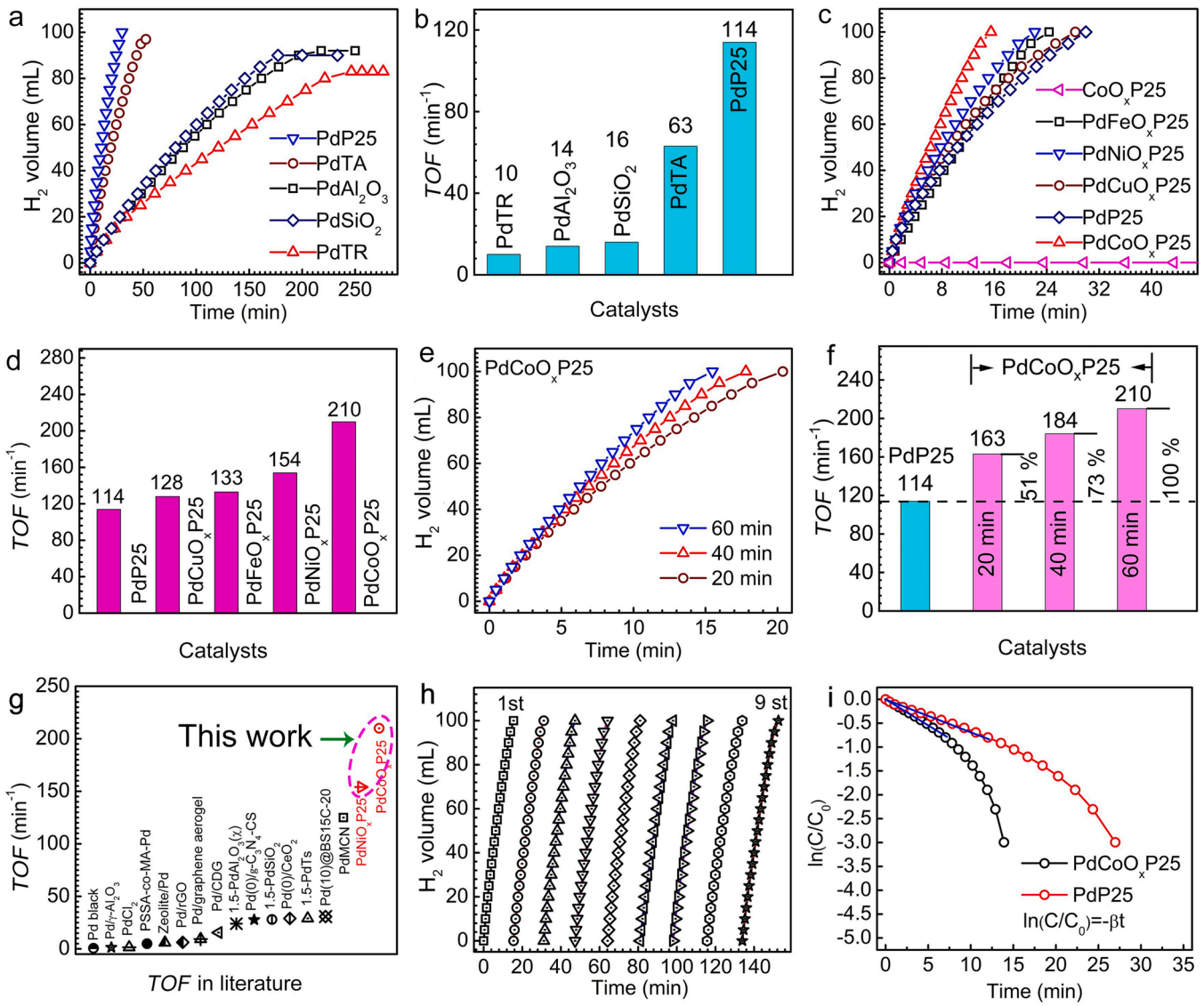

Fig. 1. (a) Hydrogen generation catalyzed by Pd catalyst with different support. (b) The corresponding *TOF* on Pd catalyst with different support. (c) Hydrogen generation catalyzed by PdP25 with different oxide nanoclusters. (d) The corresponding *TOF* on PdP25 with different oxide nanoclusters. (e) Hydrogen generation catalyzed by $PdCoO_xP25$ with different reduction time. (f) The *TOF* on $PdCoO_xP25$ with different reduction time. (g) The comparison of activity with the Pd-based catalysts in literature. (h) The cycling test of $PdCoO_xP25$ at 298 K. (i) Arrhenius plot for $PdCoO_xP25$ and PdP25.

on $PdCoO_xP25$ is far superior to the reported Pd catalysts under alkaline additive-free condition (Fig. 1 g and Table S3) [19,41–46]. It is difficult to produce hydrogen continuously for a long time in the laboratory, so the activity after several cycles is used to judge the cycle stability of the catalyst. The *TOF* remaining above 84.3 % after 9 cycles confirms an excellent cycle stability of $PdCoO_xP25$ (Fig. 1 h).

The hydrogen production from AB hydrolysis with different loading amounts of catalysts were tested at 298 K (Fig. S4a). The slope of the logarithmic curve of hydrogen generation rate versus loading amounts of $PdCoO_xP25$ is 1.14 (Fig. S4b). The above results show that AB hydrolysis is a first-order reaction to the loading amounts of $PdCoO_xP25$. Similarly, hydrogen production from different AB concentrations were tested at 298 K (Fig. S4c). The slope of the logarithmic curve of hydrogen generation rate versus AB concentrations is 0.09 (Fig. S4d). Under the specified reaction conditions, AB hydrolysis rules a zero-order reaction kinetics in a small range of concentrations (Fig. 1i). The above results show that AB hydrolysis is a zero-order reaction to AB concentrations. Therefore, *TOF* can be used instead of the reaction rate constant (k) to calculate the apparent activation energy (E_a). The E_a of AB hydrolysis on $PdCoO_x$ and $PdCoO_xP25$ is obtained via hydrogen production tests at different temperatures (Fig. S5). The analyses of reaction kinetics on the catalyst verify the significantly positive effect of coupling CoO_x and P25 in $PdCoO_xP25$ on the acceleration of AB hydrolysis.

3.2. *Structure feature*

A schematic diagram of the preparation of catalysts is given in Fig. 2a. Uniformly dispersed Pd NPs on $PdCoO_xP25$ with hetero-phase junction are observed in TEM images (Fig. 2b-d). The d spacing of 0.22 nm belonging to Pd (111) confirms the zero-valent state in Pd NPs [14]. No CoO_x NPs are observed in HAADF-STEM images of $PdCoO_xP25$ (Fig. 2b-i). The CoO_x should exist in the form of highly dispersed nanoclusters. Line-scanning EDX analysis shows a surrounded state of Pd NPs by Co element in $PdCoO_xP25$ (Fig. 2j). The above results exclude the formation of PdCo alloys (Fig. 2j) [47]. There is no difference between the crystal structure and size of Pd NPs on PdP25 and $PdCoO_xP25$ (Fig. S6a-c). The chemical composition and element dispersion of PdP25 were determined by element mapping image analysis (Fig. S6d-g). The contents of Pd in PdP25 and $PdCoO_xP25$ is close to each other (Table S1). Similar dispersion degree of Pd is detected in $PdCoO_xP25$

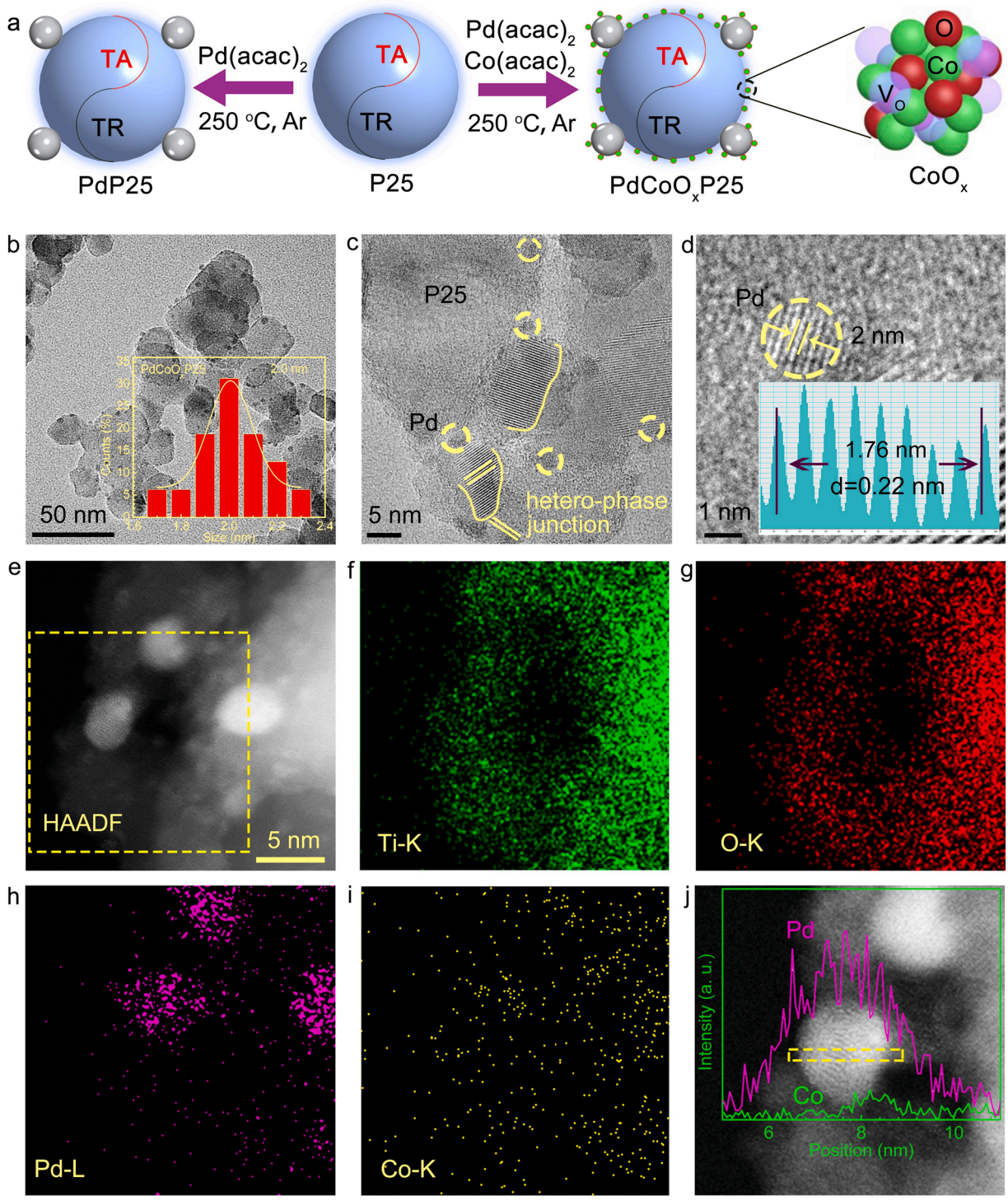

Fig. 2. (a) The schematic diagram of the preparation of catalysts. (b-d) TEM images of $PdCoO_xP25$. (e) HAADF-STEM and (f-i) EDX images of $PdCoO_xP25$. (j) The line-scanning EDX analysis of $PdCoO_xP25$.

(21.43 %) and PdP25 (25.89 %) (Table S2). From the above results, the introduction of CoO_x has no effect on the morphology of catalyst and element distribution of Pd. The unchanged microstructure of $PdCoO_xP25$ after 9 cycles (Fig. S7 and Table S1) shows an excellent stability of structure.

From similar XRD patterns, the hetero-phase junction in catalysts remains unchanged after introducing Pd and CoO_x (Fig. S8a). There is no interfacial reaction among the supports, Pd and CoO_x to generate any new component. A stronger UV absorption intensity of $PdCoO_xP25$ than PdP25 confirms the presence of V_O in CoO_x (Fig. S8b) [48]. Compared with PdP25, the EPR spectra of $PdCoO_xP25$ have a signal at $g = 2.003$ induced by the presence of V_O (Fig. 3a) [49]. With the increase of reduction time, the V_O signal intensity in $PdCoO_xP25$ shows an increasing trend (Fig. 3a). The above results confirmed that the relative concentration of V_O was positively correlated with the *TOF* on $PdCoO_xP25$ (Fig. 1 f and Fig. 3a). The increase of reduction time of $PdCoO_xP25$ has a certain limit to the improvement of *TOF* (Fig. S8c and d). There is no V_O signal in $PdFeO_xP25$, $PdCuO_xP25$ and $PdNiO_xP25$

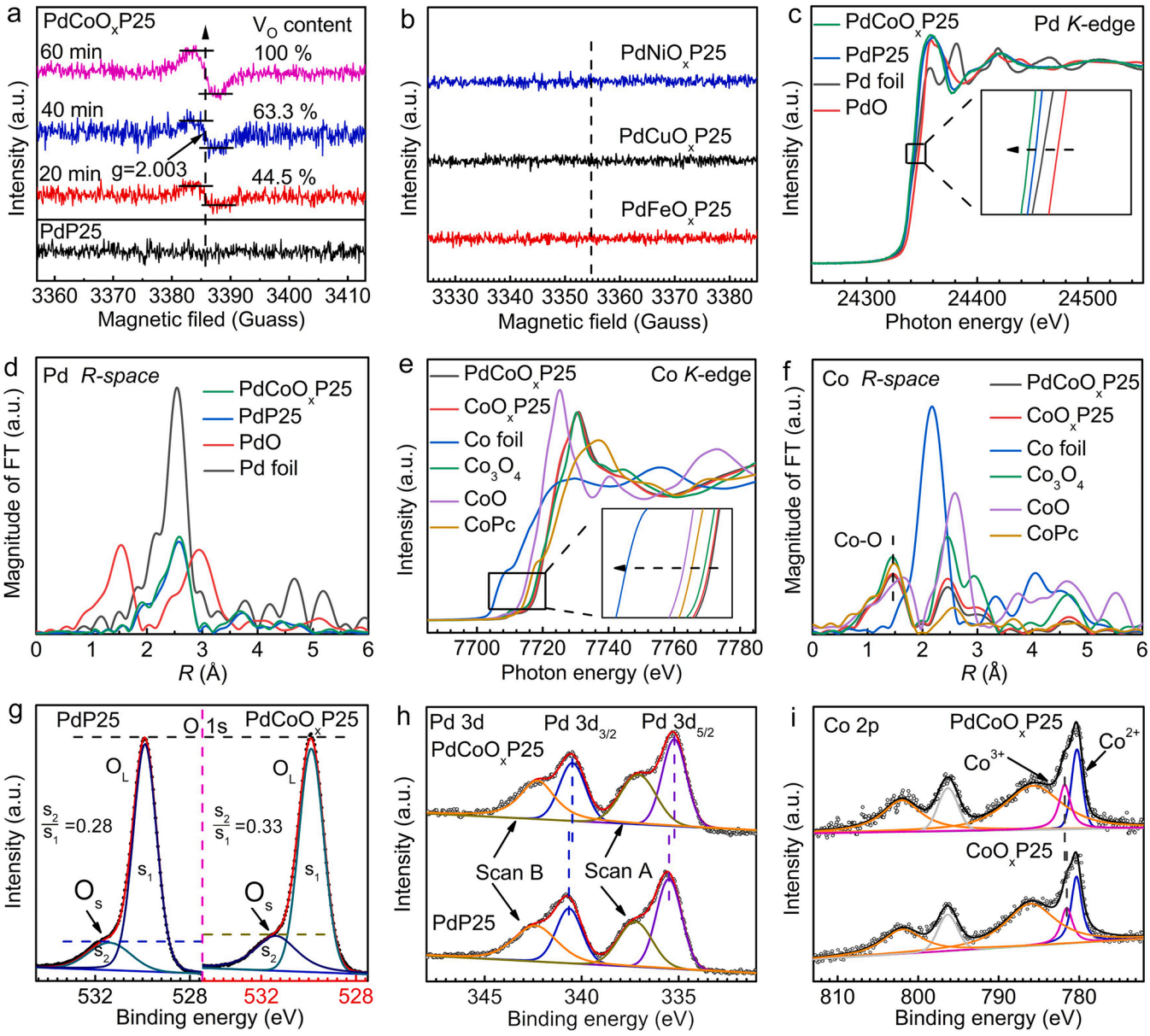

Fig. 3. (a) EPR sigal of PdCoO$_x$P25 with different V_O concentrations. (b) EPR signal of different catalysts. (c) Normalized X-ray absorption near edge structure (XANES) spectra at Pd *K*-edge for PdCoO$_x$P25, PdP25, PdO and Pd foil, respectively. (d) Extended X-ray absorption fine structure (EXAFS) spectra at Pd *K*-edge for PdCoO$_x$P25, PdP25, PdO and Pd foil in *R* spaces, respectively. (e) XANES spectra at Co *K*-edge for PdCoO$_x$P25, CoO$_x$P25, Co$_3$O$_4$, CoO, CoPc and Co foil, respectively. (f) EXAFS spectra at Co *K*-edge for PdCoO$_x$P25, CoO$_x$P25, Co$_3$O$_4$, CoO, CoPc and Co foil in *R* spaces, respectively. XPS spectra of O 1 s (g) and Pd 3d (h) in PdP25 and PdCoO$_x$P25. (i) XPS spectra of Co 2p in PdCoO$_x$P25 and CoO$_x$P25.

(Fig. 3b). Compared with PdCoO$_x$P25, the absence of V_O corresponds to the relatively low activity of PdFeO$_x$P25, PdCuO$_x$P25 and PdNiO$_x$P25. In addition, the origin of the catalytic activity of PdFeO$_x$P25, PdCuO$_x$P25 and PdNiO$_x$P25 should be understood from the electron interaction between Pd and nanoclusters [3].

The information of fine structure of Pd and Co in catalysts was revealed by XAFS. Compared with PdP25, the absorption edge of Pd in PdCoO$_x$P25 shifts to the lower energy direction (Fig. 3c). In PdCoO$_x$P25, the Pd absorption edge of lower photon energy is caused by the electron-rich sate of Pd induced by V_O in CoO$_x$ [35]. The coordination environments of Pd in PdCoO$_x$P25 and PdP25 similar to that in Pd foil confirm the metallic state of Pd (Fig. 3d). Compared with CoO$_x$P25, the absorption edge of Co in PdCoO$_x$P25 shifts to the higher photon energy direction (Fig. 3e). The coordination environment of Co in PdCoO$_x$P25 and CoO$_x$P25 similar to that in Co$_3$O$_4$ excludes the formation of metallic Co (Fig. 3 f) [35]. The above XAFS results support the electron transfer from CoO$_x$ to Pd and the formation of electron-rich Pd.

The surface composition and element valence of catalysts were detected by XPS to reveal the interactions between V_O in CoO$_x$ and surface Pd atoms. The O 1 s peaks at 530.0 eV are classified as oxygen in TiO$_2$ lattice (O$_L$) [50]. The O 1 s peak of PdP25 at 531.5 eV is classified as the oxygen species (O$_s$) adsorbed on catalyst surface [35]. The signal (531.5 eV) induced by O$_s$ in PdCoO$_x$P25 is stronger than that in PdP25 (Fig. 3 g) [51]. The stronger O$_s$ peak was attributed to the increased adsorption capacity of catalyst surface by the introduction of V_O [8]. The ratio of the area of O$_s$ (S$_2$) to the area of O$_L$ (S$_1$) in PdP25 and PdCoO$_x$P25 is 0.28 and 0.33, respectively. XPS results combined with EPR results prove the presence of V_O in PdCoO$_x$P25. The binding energies of Pd 3d$_{3/2}$ and Pd 3d$_{5/2}$ in PdP25 are 335.5 eV and 340.7 eV, respectively. The binding energies of Pd 3d$_{3/2}$ and Pd 3d$_{5/2}$ of PdCoO$_x$P25 are 335.2 eV and 340.5 eV, respectively. These information about electron state originates from the metallic Pd (Fig. 3 h) [52]. Compared with

PdP25, the lower binding energy of Pd 3d electron in $PdCoO_xP25$ confirms the electron transfer from V_O in CoO_x to Pd NPs. The XPS of Co 2p contains Co^{2+} and Co^{3+} peaks, verifying the presence of V_O in CoO_x (Fig. 3i) [23]. Compared with CoO_xP25, the increased binding energy of Co 2p electron in $PdCoO_xP25$ also verifies the electron transfer from CoO_x to Pd. The XPS results combined with the XAFS results further confirm the electron transfer from V_O in CoO_x to Pd and the construction of electron-rich Pd [53,54]. In the XPS data after $PdCoO_xP25$ cycle, the constant binding energy of each element indicates that the catalyst has excellent cyclic stability (Fig. S9).

The effect of V_O on the ability of catalyst toward water dissociation during AB hydrolysis was studied by *in situ* Raman spectra. The *in situ* Raman spectra of the catalysts before and after introducing water are shown in Fig. 4a. The catalyst has no Raman signal between 2000 and 4000 cm^{-1} before introducing water. After introducing water, the Raman peaks appeared around 3225 (ν_1) and 3450 cm^{-1} (ν_2). These two Raman peaks are attribute to the water molecules tetrahedrally (ν_1) and trihedrally (ν_2) coordinated on the catalyst surface, respectively (Fig. 4b and c) [55]. The presence of water molecules indicates an easy dissociation of water on catalyst surface. The peak (ν_1 and ν_2) intensity of water molecules in $PdCoO_xP25$ is higher than that in PdP25 (Fig. 4d). *In situ* Raman analyses confirm more water molecules adsorbed on $PdCoO_xP25$ for dissociation than that on PdP25 under the same conditions [55]. This result directly supports the formation of electron-rich Pd caused by V_O and the promotion in the adsorption and dissociation of water molecules.

To confirm the potential of coupling V_O and hetero-phase junction to promote O-H bond breaking, hydrogen production from AB methanolysis was performed at room temperature. The hetero-phase junction in P25 is beneficial to the pre-adsorption of AB and CH_3OH molecules. The optimized pre-adsorption results in a higher catalytic activity of PdP25 (Fig. S10a). The relative concentration of V_O in catalyst increased *TOF* in the same trend as AB hydrolysis reaction (Fig. S10b and c). The above results further confirm the potential of coupling V_O and hetero-phase junction in AB hydrogen evolution reactions.

3.3. Catalytic mechanism

The effect of V_O and P25 on the improvement of catalytic activity of Pd catalyst and corresponding catalytic mechanism in AB hydrolysis is studied through DFT simulation. The AB hydrolysis is supposed to undergo a multistep process composed of bimolecular reactions. Considering the complicate nature of evolution reaction process and the effect of spatial distribution of active sites on the molecular activation, the activation of water and AB on Pd NPs, Pd/TiO_2, $Pd\text{-}CoO_x$ and $CoO_x\text{-}Pd/TiO_2$ (Fig. 5a-d and Fig. S11) are investigated separately [56]. Because monodisperse CoO_x nanoclusters with the same amount of Pd plays a role of electron promoter rather than support, the contribution of metal-support to catalytic activity was excluded (Fig. S1 and Fig. S2a-b) [57–59]. CoO_x is distributed around Pd in the form of subnanometer clusters. The DFT simulation based on the model of intimate contact between CoO_x and Pd is reliable for the real states and catalytic process. The activation energy of water molecule on Pd (1.28 eV), Pd/TiO_2 (0.93 eV), $Pd\text{-}CoO_x$ (0.79 eV) and $CoO_x\text{-}Pd/TiO_2$ (0.56 eV) show a

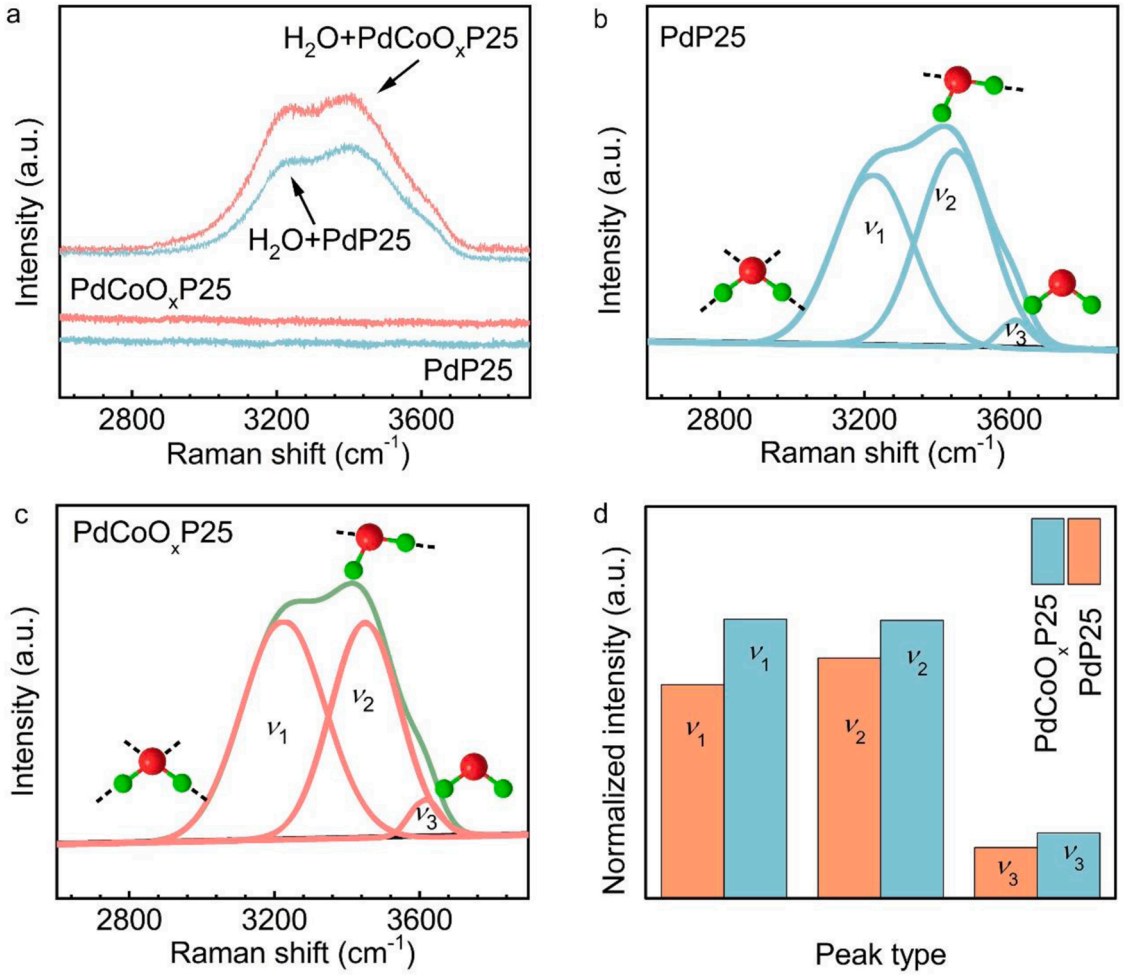

Fig. 4. (a) The *in situ* Raman spectra of the catalysts before and after introducing water. (b, c) Raman peaks of water on the surface of catalysts. (d) The normalized intensity of Raman signal of water on the surface of catalysts.

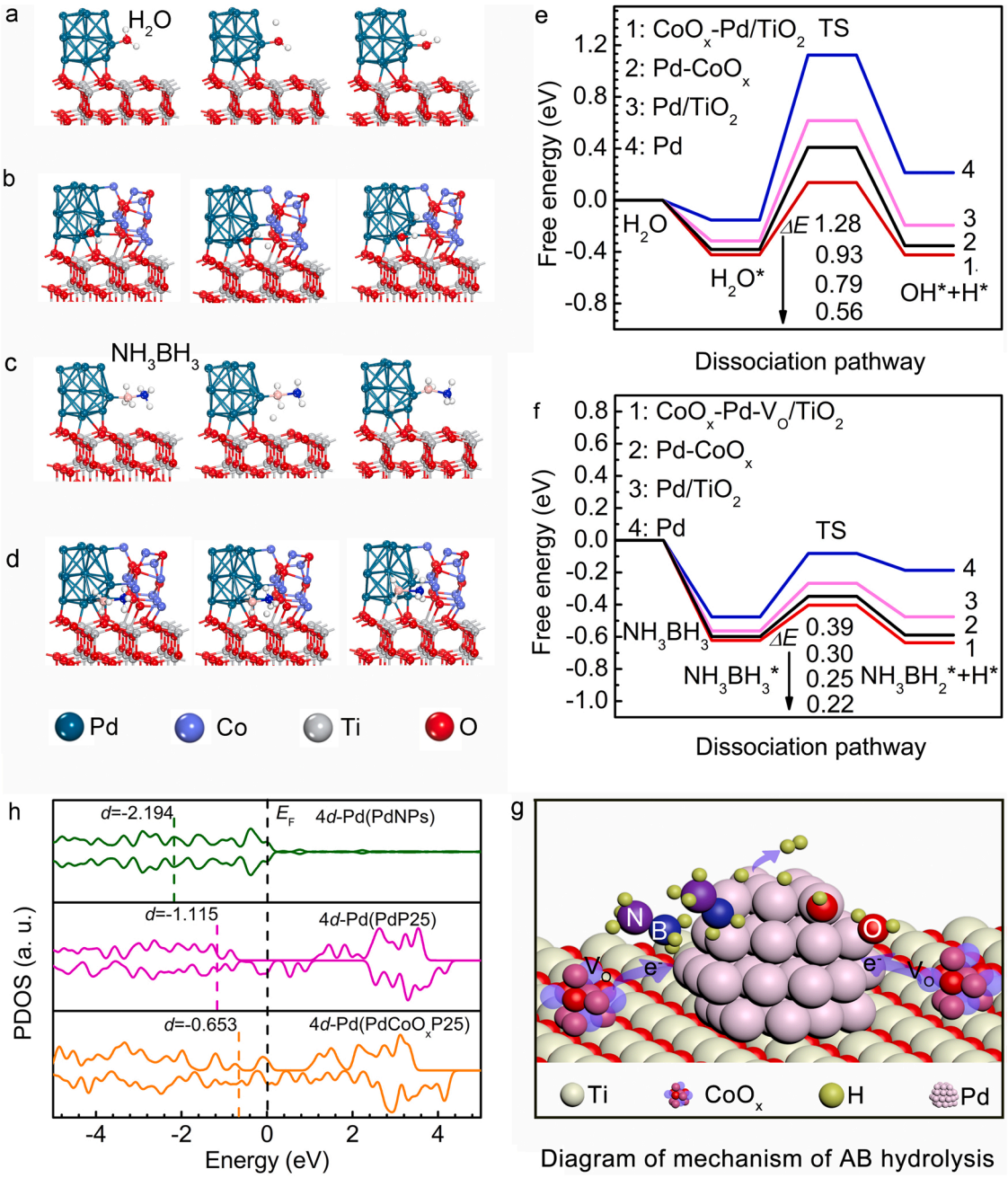

Fig. 5. The path of water dissociation on (a) Pd/TiO_2 and (b) CoO_x-Pd/TiO_2. The path of AB dissociation on (c) Pd/TiO_2 and (d) CoO_x-Pd/TiO_2. Gibbs free energy diagrams of adsorption, activation, and dissociation for (e) H_2O and (f) AB on Pd, Pd/TiO_2, Pd-CoO_x and CoO_x-Pd/TiO_2, respectively. (g) The PDOS of Pd 4*d* in Pd NPs, PdP25 and $PdCoO_xP25$. (h) Diagram of mechanism of AB hydrolysis.

decreasing tendency (Fig. 5e). The activation energy of AB molecule on Pd (0.39 eV), Pd/TiO_2 (0.30 eV), Pd-CoO_x (0.25 eV) and CoO_x-Pd/TiO_2 (0.22 eV) also show a decreasing tendency (Fig. 5f). The DFT simulation confirm that water dissociation is the RLS in AB hydrolysis on these catalysts. The DFT calculation of AB methanolysis also confirms that the breaking of O-H is RLS step (Fig. S12). Due to steric hindrance effect, the activation energy of CH_3OH is higher than that of H_2O. The higher activation energy is the reason that the activity of AB hydrolysis is higher than that of AB methanolysis. The activation energies of water and AB are obviously reduced after introducing V_O into PdP25 [60]. For the main model, the partial densities of states (PDOS) of 4*d* band in Pd NPs (−2.194 eV), PdP25 (−1.156 eV) and $PdCoO_xP25$ (−0.653 eV) show an increasing tendency in the *d*-band center of Pd. Combining the XPS and PDOS results, the increasing 4*d* band center of Pd indicates the enhancement of electron-rich state (Fig. 5g). The 4*d* orbital of electron-rich Pd caused by V_O in CoO_x tends to overlap the anti-bond orbital of O-H bond in water. The strength of O-H bond is weakened and easier to break [61]. The experimental results and DFT simulation show that the coupling of V_O and hetero-phase junction modulate the electronic structure of Pd. The activation of reactant molecules and the breaking of the bonds are enhanced by the modulation [62–66].

Due to the thermodynamic deficiency of direct water dissociation, a pre-activation caused by acid-base interaction between the adsorbed water molecule and the partially dissociated AB molecule is necessary for complete water dissociation. The main mechanisms of AB hydrolysis also include a simultaneous dissociation of two reactant molecules and the interaction between two activated molecules [56,65]. Based on the above analysis, a dissociation-interaction mechanism of AB hydrolysis

on $PdCoO_xP25$ is proposed (Fig. 5h). The specific reaction pathways are as the follows:

$$NH_3BH_3+2Pd^*=Pd\text{-}NH_3BH_2^*+Pd\text{-}H^* \quad (4)$$

$$H_2O+2Pd^*=Pd\text{-}OH^*+Pd\text{-}H^* \quad (5)$$

$$Pd\text{-}NH_3BH_2^*+Pd\text{-}H^*+Pd\text{-}OH^*+Pd\text{-}H^*=Pd\text{-}NH_3BH_2OH^*+H_2+3Pd^* \quad (6)$$

$$Pd\text{-}NH_3BH_2OH^*+Pd\text{-}OH^*+Pd\text{-}H^*=PdNH_3BH(OH)_2^*+H_2+2Pd^* \quad (7)$$

$$Pd\text{-}NH_3BH(OH)_2^*=Pd\text{-}NH_3BHO^*+H_2O \quad (8)$$

$$Pd\text{-}NH_3BHO^*+Pd\text{-}OH^*+Pd\text{-}H^*=Pd\text{-}NH_3BOOH^*+H_2+2Pd^* \quad (9)$$

$$Pd\text{-}NH_3BOOH^*=NH_4^++BO_2^-+Pd^* \quad (10)$$

In the first stage of dehydrogenation process, the hydrolysis of AB involves two steps, namely, an oxidation addition and a reductive elimination [56,57]. AB and water molecules dissociate on the surface of catalyst through an oxidation addition along with a pre-activation between AB and water. The surface species react further with each other by a reduction elimination to form hydrogen molecules and new intermediates. In the dissociation stage, AB and water molecules undergo an oxidation addition onto the surface Pd atoms to generate hydrogen atom, NH_3BH_2 and OH radicals. In the reaction and desorption stage, two desorbed hydrogen atoms combine into one hydrogen molecules to desorb from the surface of catalyst. A H_2O is adsorbed on Pd atom through an O-H bond, and then dissociates to form Pd-H* and Pd-OH*. An NH_3BH_3 adsorbs on Pd atom through a B-H bond, and then dissociates to form Pd-H* and $Pd\text{-}NH_3BH_2^*$. The Pd-OH* attacks $Pd\text{-}NH_3BH_2^*$ and forms NH_3BH_2OH. Finally, two Pd-H* combine into the first H_2 in Pd surface and breaks away. The remaining two H_2 precipitate from the Pd surface in the same process (Eq. 4-Eq. 10). The hydrolysate products of AB are NH_4^+, BO_2^- and H_2. Although the dissociation of B-H and O-H bonds and the pre-activation of H_2O have been discussed in V_O and hetero-phase junction coupling system, the sequence of the formation of H-H and B-O still requires a satisfactory solution. Further detailed theoretical analysis and ultrafast *in situ* velocity spectroscopic studies are needed to confirm or exclude the existence of intermediate or transition states of four-membered rings.

4. Conclusions

In summary, the feasibility of coupling V_O and hetero-phase junction to boost water dissociation is confirmed in AB hydrolysis at room temperature. The outstanding *TOF* (210 min^{-1} calculated based on the overall Pd content, 981 min^{-1} calculated based on dispersion degree of Pd) is achieved on the optimized $PdCoO_xP25$ catalyst. The experimental results and DFT simulation confirm that both the appropriate interfacial charge states benefitting for adsorption caused by hetero-phase junction and the electron-rich Pd caused by V_O enhance the intrinsic catalytic activity of Pd toward water dissociation in AB hydrolysis. The 4*d* orbital of electron-rich Pd caused by V_O in CoO_x tends to overlap the anti-bond orbital of O-H bond in water. The stability of O-H bond in water molecule decreases and easier to break. Coupling V_O and hetero-phase junction to promote O-H bond breaking has also been demonstrated in AB methanolysis. This proof-of-concept achievement demonstrates the potential of coupling V_O and hetero-phase junction in the design of catalysts for important conversion of energy and resources. The problem of water dissociation in the field of heterogeneous catalysis can be resolved by some inspirations from this research.

CRediT authorship contribution statement

Ruofan Shen: Investigation, Visualization, Writing – original draft, Writing – review & editing, Formal analysis. **Yanyan Liu:** Investigation, Conceptualization, Supervision. **Huanhuan Zhang:** Investigation. **Shuling Liu:** Investigation. **Huijuan Wei:** Investigation. **Huiyu Yuan:** Investigation. **Hao Wen:** Investigation. **Xianli Wu:** Investigation, Funding acquisition. **Sehrish Mehdi:** Investigation. **Tao Liu:** Investigation. **Jianchun Jiang:** Investigation, Supervision. **Erjun Liang:** Visualization, Formal analysis, Supervision, Funding acquisition. **Baojun Li:** Formal analysis, Supervision, Conceptualization, Funding acquisition.

Declaration of Competing Interest

The authors declare that they have no known competing financial interests or personal relationships that could have appeared to influence the work reported in this paper.

Data availability

No data was used for the research described in the article.

Acknowledgement

This work was supported by the National Natural Science Foundation of China (No. 22279118, No. 11874328, No. 22075254).

Appendix A. Supporting information

Supplementary data associated with this article can be found in the online version at doi:10.1016/j.apcatb.2023.122484.

References

[1] X. Sun, X. Luo, S. Jin, X. Zhang, H. Wang, W. Shao, X. Wu, Y. Xie, Surface modification of $ZnIn_2S_4$ layers to realise energy transfer-mediated photocatalysis, Natl. Sci. Rev. 10 (2022), nwac026, https://doi.org/10.1093/nsr/nwac026.

[2] S. Yao, Z. Xiao, Z. Wu, G. Rui, W. Xu, Y. Ye, L. Lin, X. Wen, P. Liu, B. Chen, Atomic-layered Au clusters on α-MoC as catalysts for the low-temperature water-gas shift reaction, Sci. Found. China 357 (2017) 389, https://doi.org/10.1126/science.aah4321.

[3] R. Shen, Y. Liu, H. Wen, X. Wu, G. Han, X. Yue, S. Mehdi, T. Liu, H. Cao, E. Liang, B. Li, Engineering bimodal oxygen vacancies and Pt to boost the activity toward water dissociation, Small 18 (2021) 2105588, https://doi.org/10.1002/smll.202105588.

[4] L. Lin, W. Zhou, R. Gao, S. Yao, X. Zhang, W. Xu, S. Zheng, Z. Jiang, Q. Yu, Y. Li, C. Shi, X. Wen, D. Ma, Low-temperature hydrogen production from water and methanol using Pt/α-MoC catalysts, Nature 544 (2017) 80–83, https://doi.org/10.1038/nature21672.

[5] Q. Yao, Z. Lu, Y. Yang, Y. Chen, X. Chen, H. Jiang, Facile synthesis of graphene-supported Ni-CeO_x nanocomposites as highly efficient catalysts for hydrolytic dehydrogenation of ammonia borane, Nano Res. 11 (2018) 4412–4422, https://doi.org/10.1007/s12274-018-2031-y.

[6] F. Zhang, C. Ma, Y. Zhang, H. Li, D. Fu, X. Du, X. Zhang, N-doped mesoporous carbon embedded Co nanoparticles for highly efficient and stable H_2 generation from hydrolysis of ammonia borane, J. Power Sources 399 (2018) 89–97, https://doi.org/10.1016/j.jpowsour.2018.07.069.

[7] F. Fu, C. Wang, Q. Wang, A.M. Martinez-Villacorta, A. Escobar, H. Chong, X. Wang, S. Moya, L. Salmon, E. Fouquet, J. Ruiz, D. Astruc, Highly selective and sharp volcano-type synergistic Ni_2Pt@ZIF-8-catalyzed hydrogen evolution from ammonia borane hydrolysis, J. Am. Chem. Soc. 140 (2018) 10034–10042, https://doi.org/10.1021/jacs.8b06511.

[8] R. Shen, Y. Liu, H. Wen, X. Wu, Z. Peng, S. Mehdi, T. Liu, H. Zhang, S. Guan, E. Liang, B. Li, Engineering vacancy-atom ensembles to boost catalytic activity toward hydrogen evolution, Energy Environ. Mater. 6 (2023), e12292, https://doi.org/10.1002/eem2.12292.

[9] Y. Liu, G. Han, X. Zhang, C. Xing, C. Du, H. Cao, B. Li, Co-Co_3O_4@carbon core–shells derived from metalorganic framework nanocrystals as efficient hydrogen evolution catalysts, Nano Res. 10 (2017) 3035–3548, https://doi.org/10.1007/s12274-017-1519-1.

[10] J. Manna, S. Akbayrak, S. Zkar, Palladium(0) nanoparticles supported on polydopamine coated $CoFe_2O_4$ as highly active, magnetically isolable and reusable catalyst for hydrogen generation from the hydrolysis of ammonia borane, Appl. Catal. B Environ. 208 (2017) 104–115, https://doi.org/10.1016/j.apcatb.2017.02.037.

[11] Z. Li, T. He, D. Matsumura, S. Miao, A. Wu, L. Liu, G. Wu, P. Chen, Atomically dispersed Pt on the surface of Ni particles: synthesis and catalytic function in hydrogen generation from aqueous ammonia-borane, ACS Catal. 7 (2017) 6762–6769, https://doi.org/10.1021/acscatal.7b01790.

[12] L. Wang, H. Li, W. Zhang, X. Zhao, J. Qiu, A. Li, X. Zheng, Z. Hu, R. Si, J. Zeng, Supported rhodium catalysts for ammonia-borane hydrolysis: dependence of the

catalytic activity on the highest occupied state of the single rhodium atoms, Angew. Chem. 129 (2017) 4790–4796, https://doi.org/10.1002/ange.201701089.
[13] Y. Wang, G. Shen, Y. Zhang, L. Pan, X. Zhang, J.-J. Zou, Visible-light-induced unbalanced charge on NiCoP/TiO_2 sensitized system for rapid H_2 generation from hydrolysis of ammonia borane, Appl. Catal. B Environ. 260 (2020), 118183, https://doi.org/10.1016/j.apcatb.2019.118183.
[14] F. Yao, S. Guan, L. Bian, Y. Fan, X. Liu, H. Zhang, B. Li, B. Liu, Ensemble-exciting effect in Pd/alk-Ti_3C_2 on the activity for efficient hydrogen production, ACS Sustain, Chem. Eng. 9 (2021) 12332–12340, https://doi.org/10.1021/acssuschemeng.1c04249.
[15] R. Tahawy, E. Doustkhah, E.S.A. Abdel-Aal, M. Esmat, F.E. Farghaly, H. El-Hosainy, N. Tsunoji, F.I. El-Hosiny, Y. Yamauchi, M.H.N. Assadi, Y. Ide, Exceptionally stable green rust, a mixed-valent iron-layered double hydroxide, as an efficient solar photocatalyst for H_2 production from ammonia borane, Appl. Catal. B Environ. 286 (2021), 119854, https://doi.org/10.1016/j.apcatb.2020.119854.
[16] Y. Ge, X. Qin, A. Li, Y. Deng, L. Lin, M. Zhang, Q. Yu, S. Li, M. Peng, Y. Xu, X. Zhao, M. Xu, W. Zhou, S. Yao, D. Ma, Maximizing the synergistic effect of CoNi catalyst on α-MoC for robust hydrogen production, J. Am. Chem. Soc. 143 (2021) 628–633, https://doi.org/10.1021/jacs.0c11285.
[17] Q. Sun, N. Wang, Q. Xu, J. Yu, Nanopore-supported metal nanocatalysts for efficient hydrogen generation from liquid-phase chemical hydrogen storage materials, Adv. Mater. 32 (2020), 2001818, https://doi.org/10.1002/adma.202001818.
[18] H. Zhang, Y. Liu, H. Wei, C. Wang, T. Liu, X. Wu, S. Ashraf, S. Mehdi, S. Guan, Y. Fan, X. Yue, B. Liu, Y. Zhang, H. Cao, B. Li, Atomic-bridge structure in B-Co-P dual-active sites on boron nitride nanosheets for catalytic hydrogen generation, Appl. Catal. B Environ. 314 (2022), 121495, https://doi.org/10.1016/j.apcatb.2022.121495.
[19] X. Qiu, X. Wu, Y. Wu, Q. Liu, C. Huang, The release of hydrogen from ammonia borane over copper/hexagonal boron nitride composites, RSC Adv. 6 (2016) 106211–106217, https://doi.org/10.1039/C6RA24000C.
[20] X. Huang, Y. Liu, H. Wen, R. Shen, S. Mehdi, X. Wu, E. Liang, X. Guo, B. Li, Ensemble-boosting effect of Ru-Cu alloy on catalytic activity towards hydrogen evolution in ammonia borane hydrolysis, Appl. Catal. B Environ. 287 (2021), 119960, https://doi.org/10.1016/j.apcatb.2021.119960.
[21] P. Li, R. Chen, S. Zhao, W. Li, Y. Lin, Y. Yu, Architecture control and electronic structure engineering over Ni-based nitride nanocomposite for boosting ammonia borane dehydrogenation, Appl. Catal. B Environ. 298 (2021), 120523, https://doi.org/10.1016/j.apcatb.2021.120523.
[22] A. Bulut, M. Yuederi, İ. Ertas, M. Celebi, M. Kaya, M. Zahmakiran, Carbon dispersed copper-cobalt alloy nanoparticles: a cost-effective heterogeneous catalyst with exceptional performance in the hydrolytic dehydrogenation of ammonia-borane, Appl. Catal. B Environ. 269 (2020), 118775, https://doi.org/10.1016/j.apcatb.2020.118775.
[23] S. Guan, L. An, S. Ashraf, L. Zhang, B. Liu, Y. Fan, B. Li, Oxygen vacancy excites Co_3O_4 nanocrystals embedded into carbon nitride for accelerated hydrogen generation, Appl. Catal. B Environ. 269 (2020), 118775, https://doi.org/10.1016/j.apcatb.2020.118775.
[24] Y. Tonbul, S. Akbayrak, S. Özkar, Palladium(0) nanoparticles supported on ceria: highly active and reusable catalyst in hydrogen generation from the hydrolysis of ammonia borane, Int. J. Hydrog. Energy 41 (2016) 11154–11162, https://doi.org/10.1016/j.ijhydene.2016.04.058.
[25] K. Lin, S. Ju, H. Chen, H. Chen, M. Weng, J. Lin, J. Hsieh, S. Yung, W. Huang, Density function theory study on adsorption and dissociation of H_2O on Pd nanowire, J. Nanosci. Nanotechnol. 13 (2013), 813–8, https://doi.org/10.1166/jnn.2013.6124.
[26] J. Zhu, Y. Guo, F. Liu, H. Xu, L. Gong, W. Shi, D. Chen, P. Wang, Y. Yang, C. Zhang, J. Wu, J. Luo, S. Mu, Regulative electronic states around ruthenium/ruthenium disulphide heterointerfaces for efficient water splitting in acidic media, Angew. Chem. 60 (2021) 12328–12334, https://doi.org/10.1002/anie.202101539.
[27] D. Chen, R. Lu, R. Yu, Y. Dai, H. Zhao, D. Wu, P. Wang, J. Zhu, Z. Pu, L. Chen, J. Yu, S. Mu, Work-function-induced interfacial built-in electric fields in Os-$OsSe_2$ heterostructures for active acidic and alkaline hydrogen evolution, Angew. Chem. 61 (2022), e202208642, https://doi.org/10.1002/anie.202208642.
[28] J. Zhu, F. Xia, Y. Guo, R. Lu, L. Gong, D. Chen, P. Wang, L. Chen, J. Yu, J. Wu, S. Mu, Electron accumulation effect over osmium/erlichmanite heterointerfaces for intensified pH-universal hydrogen evolution, ACS Catal. 12 (2022) 13312–13320, https://doi.org/10.1021/acscatal.2c03102.
[29] J. Zhu, R. Lu, W. Shi, L. Gong, D. Chen, P. Wang, L. Chen, J. Wu, S. Mu, Y. Zhao, Epitaxially grown Ru clusters–nickel nitride heterostructure advances water electrolysis kinetics in alkaline and seawater media, Energy Environ. Mater. (2022), https://doi.org/10.1002/anie.202208642.
[30] X. Dong, W. Cui, H. Wang, J. Li, Y. Sun, H. Wang, Y. Zhang, H. Huang, F. Dong, Promoting ring-opening efficiency for suppressing toxic intermediates during photocatalytic toluene degradation via surface oxygen vacancies, Sci. Bull. 64 (2019) 669–678, https://doi.org/10.1016/j.scib.2019.04.020.
[31] N. Yao, R. Meng, F. Wu, Z. Fan, G. Cheng, W. Luo, Oxygen-vacancy-induced CeO_2/Co_4N heterostructures toward enhanced pH-Universal hydrogen evolution reactions, Appl. Catal. B Environ. 277 (2020), 119282, https://doi.org/10.1016/j.apcatb.2020.119282.
[32] F. Luo, R. Xu, S. Ma, Q. Zhang, H. Hu, K. Qu, S. Xiao, Z. Yang, W. Cai, Engineering oxygen vacancies of cobalt tungstate nanoparticles enable efficient water splitting in alkaline medium, Appl. Catal. B Environ. 259 (2019), 118090, https://doi.org/10.1016/j.apcatb.2019.118090.
[33] H. Lin, H. Huang, Y. Zhang, T. Ma, Oxygen vacant semiconductor photocatalysts, Adv. Funct. Mater. 31 (2021), 2100919, https://doi.org/10.1002/adfm.202100919.
[34] Y. Zhang, X. Yang, X. Yang, H. Duan, H. Qi, Y. Su, B. Liang, H. Tao, B. Liu, D. Chen, X. Su, Y. Huang, T. Zhang, Tuning reactivity of Fischer–Tropschsynthesis by regulating TiO_x overlayer over Ru/TiO_2 nanocatalysts, Nat. Commun. 11 (2020) 3185, https://doi.org/10.1038/s41467-020-17044-4.
[35] R. Shen, Y. Liu, H. Wen, T. Liu, Z. Peng, X. Wu, X. Ge, S. Mehdi, H. Cao, E. Liang, J. Jiang, B. Li, Engineering V_O-Ti ensemble to boost the activity of Ru towards water dissociation for catalytic hydrogen generation, Appl. Catal. B Environ. 306 (2022), 121100, https://doi.org/10.1016/j.apcatb.2022.121100.
[36] J. Huang, H. Sheng, D. Ross, J. Han, X. Wang, B. Song, S. Jin, Modifying redox properties and local bonding of Co_3O_4 by CeO_2 enhances oxygen evolution catalysis in acid, Nat. Commun. 12 (2021) 3036, https://doi.org/10.1038/s41467-021-23390-8.
[37] Y. Zhou, Z. Zhao, Interfacial structure and properties of TiO_2 phase junction studied by DFT calculations, Appl. Surf. Sci. 485 (2019) 8–21, https://doi.org/10.1016/j.apsusc.2019.04.193.
[38] J. Kim, C. Rong, Y. Lee, J.P. Liu, S. Sun, From core/shell structured FePt/Fe_3O_4/MgO to ferromagnetic FePt nanoparticles, Chem. Mater. 20 (2008) 7242–7245, https://doi.org/10.1021/cm8024878.
[39] G. Yang, S. Guan, S. Mehdi, Y. Fan, B. Liu, B. Li, Co-CoO_x supported onto TiO_2 coated with carbon as a catalyst for efficient and stable hydrogen generation from ammonia borane, Green. Energy Environ. 6 (2021) 236–243, https://doi.org/10.1016/j.gee.2020.03.012.
[40] J. Liao, Y. Shao, Y. Feng, J. Zhang, C. Song, W. Zeng, J. Tang, H. Dong, Q. Liu, H. Li, Interfacial charge transfer induced dual-active-sites of heterostructured $Cu_{0.8}Ni_{0.2}WO_4$ nanoparticles in ammonia borane methanolysis for fast hydrogen production, Appl. Catal. B Environ. 320 (2023) 121973. https://doi.org/10.1016/j.apcatb.2022.121973.
[41] S. Akbayrak, M. Kaya, M. Volkan, S. Özkar, Palladium(0) nanoparticles supported on silica-coated cobalt ferrite: a highly active, magnetically isolable and reusable catalyst for hydrolytic dehydrogenation of ammonia borane, Appl. Catal. B Environ. 147 (2014) 387–393, https://doi.org/10.1016/j.apcatb.2013.09.023.
[42] W. Wang, Z. Lu, Y. Luo, A. Zou, Q. Yao, X. Chen, Mesoporous carbon nitride supported Pd and Pd-Ni nanoparticles as highly efficient catalyst for catalytic hydrolysis of NH_3BH_3, ChemCatChem 10 (2018) 1620–1626, https://doi.org/10.1002/cctc.201701989.
[43] H. Jia, X. Chen, X. Song, X. Zheng, X. Guan, P. Liu, Graphitic carbon nitride-chitosan composites–anchored palladium nanoparticles as high-performance catalyst for ammonia borane hydrolysis, Int. J. Energy Res. 43 (2019) 535–543, https://doi.org/10.1002/er.4290.
[44] P. Xi, F. Chen, G. Xie, C. Ma, H. Liu, C. Shao, J. Wang, Z. Xu, X. Xu, Z. Zeng, Surfactant free RGO/Pd nanocomposites as highly active heterogeneous catalysts for the hydrolytic dehydrogenation of ammonia borane for chemical hydrogen storage, Nanoscale 4 (2012) 5597–5601, https://doi.org/10.1039/c2nr31010d.
[45] P. Ramachandran, P. Gagare, Preparation of ammonia borane in high yield and purity, methanolysis, and regeneration, Inorg. Chem. 46 (2007) 7810–7817, https://doi.org/10.1021/ic700772a.
[46] M. Chandra, Q. Xu, Room temperature hydrogen generation from aqueous ammonia-borane using noble metal nano-clusters as highly active catalysts, J. Power Sources 168 (2007) 135–142, https://doi.org/10.1016/j.jpowsour.2007.03.015.
[47] Y. Liu, X. Li, Q. Zhang, W. Li, Y. Xie, H. Liu, L. Shang, Z. Liu, Z. Chen, L. Gu, Z. Tang, T. Zhang, S. Lu, A general route to prepare low-ruthenium-content bimetallic electrocatalysts for pH-universal hydrogen evolution reaction by using carbon quantum dots, Angew. Chem. 132 (2020) 1735–1743, https://doi.org/10.1002/ange.201913910.
[48] G. Zhuang, Y. Chen, Z. Zhuang, Y. Yu, J. Yu, Oxygen vacancies in metal oxides: recent progress towards advanced catalyst design, Sci. China Mater. 63 (2020) 2089–2118, https://doi.org/10.1007/s40843-020-1305-6.
[49] M. Liang, X. Li, L. Jiang, P. Ran, H. Wang, X. Chen, C. Xu, M. Tian, S. Wang, J. Zhang, T. Cui, L. Qu, Femtosecond laser mediated fabrication of micro/nanostructured TiO_2-photoelectrodes: hierarchical nanotubes array with oxygen vacancies and their photocatalysis properties, Appl. Catal. B Environ. 277 (2020), 119231, https://doi.org/10.1016/j.apcatb.2020.119231.
[50] X. Chen, X. Zhang, Y. Li, M. Qi, J. Li, Z. Tang, Z. Zhou, Y. Xu, Transition metal doping BiOBr nanosheets with oxygen vacancy and exposed {102} facets for visible light nitrogen fixation, Appl. Catal. B Environ. 281 (2021), 119516, https://doi.org/10.1016/j.apcatb.2020.119516.
[51] J. Li, M. Zhang, Z. Guan, Q. Li, C. He, J. Yang, Synergistic effect of surface and bulk single-electron-trapped oxygen vacancy of TiO_2 in the photocatalytic reduction of CO_2, Appl. Catal. B Environ. 206 (2017) 300–307, https://doi.org/10.1016/j.apcatb.2017.01.025.
[52] J. Li, H. Zhou, H. Zhuo, Z. Wei, G. Zhuang, X. Zhong, S. Deng, X. Li, J. Wang, Oxygen vacancies on TiO_2 promoted the activity and stability of supported Pd nanoparticles for the oxygen reduction reaction, J. Mater. Chem. A 6 (2018) 2264–2272, https://doi.org/10.1039/C7TA09831F.
[53] J.W. Niemantsverdriet, J.W. Niemantsverdriet. Concepts of modern catalysis and kinetics, Wiley-VCH Verlag GmbH, Weinheim, 2003.
[54] L. Pauling, The nature of the chemical bond, Cornell University Press, New York, 1960.
[55] J. Zhu, H. Yang, W. Zhang, Y. Mao, S. Lyu, J. Chen, An In situ Raman study of intermediate adsorption engineering by high-index facet control during the hydrogen evolution reaction, Inorg. Chem. Front. 7 (2020) 1892–1899, https://doi.org/10.1039/D0QI00124D.

[56] N. Kang, X. Wei, R. Shen, B. Li, E. Cal, S. Moya, L. Salmon, C. Wang, E. Coy, M. Berlande, J. Pozzo, D. Astruc, Fast Au-Ni@ZIF-8-catalyzed ammonia borane hydrolysis boosted by dramatic volcano-type synergy and plasmonic acceleration, Appl. Catal. B Environ. 320 (2023), 121957, https://doi.org/10.1016/j.apcatb.2022.121957.

[57] C. Wang, Q. Wang, F. Fu, D. Astruc, Hydrogen generation upon nanocatalyzed hydrolysis of hydrogen-rich boron derivatives: recent developments, Acc. Chem. Res. 53 (2020) 2483–2493, https://doi.org/10.1021/acs.accounts.0c00525.

[58] J. Li, Q. Guan, H. Wu, W. Liu, Y. Lin, Z. Sun, X. Ye, X. Zheng, H. Pan, J. Zhu, S. Chen, W. Zhang, S. Wei, J. Lu, Highly active and stable metal single-atom catalysts achieved by strong electronic metal–support interactions, J. Am. Chem. Soc. 141 (2019) 14515–14519, https://doi.org/10.1021/jacs.9b06482.

[59] S. Akbayrak, S. Özkar, Magnetically isolable Pt^0/Co_3O_4 nanocatalysts: outstanding catalytic activity and high reusability in hydrolytic dehydrogenation of ammonia borane, ACS Appl. Mater. Interfaces 13 (2021) 34341–34348, https://doi.org/10.1021/acsami.1c08362.

[60] C. Wang, Y. Ren, J. Zhao, S. Sun, X. Du, M. Wang, G. Ma, H. Yu, L. Li, X. Yu, X. Zhang, Z. Lu, X. Yang, Oxygen vacancy-attired dual-active-sites Cu/$Cu_{0.76}Co_{2.24}O_4$ drives electron transfer for efficient ammonia borane dehydrogenation, Appl. Catal. B Environ. 314 (2022), 121494, https://doi.org/10.1016/j.apcatb.2022.121494.

[61] S. Akbayrak, S. Özkar, Palladium nanoparticles supported on cobalt(II,III) oxide nanocatalyst: high reusability and outstanding catalytic activity in hydrolytic dehydrogenation of ammonia borane, J. Colloid Interface Sci. 626 (2022) 752–758, https://doi.org/10.1016/j.jcis.2022.06.135.

[62] Y. Liu, H. Wen, D. Zhou, X. Huang, X. Wu, J. Jiang, X. Guo, B. Li, Tuning surface *d* charge of Ni-Ru alloys for unprecedented catalytic activity towards hydrogen generation from ammonia borane hydrolysis, Appl. Catal. B Environ. 291 (2021), 120094, https://doi.org/10.1016/j.apcatb.2021.120094.

[63] S. Zhang, C. Chang, Z. Huang, Y. Ma, W. Gao, J. Li, Y. Qu, Visible-light-activated suzuki–miyaura coupling reactions of aryl chlorides over the multifunctional Pd/Au/porous nanorods of CeO_2 catalysts, ACS Catal. 5 (2015) 6481–6488, https://doi.org/10.1021/acscatal.5b01173.

[64] S. Zou, B. Lou, K. Yang, W. Yuan, C. Zhu, Y. Zhu, Y. Du, L. Lu, J. Liu, W. Huang, B. Yang, Z. Gong, Y. Cui, Y. Wang, L. Ma, J. Ma, Z. Jiang, L. Xiao, J. Fan, Grafting nanometer metal/oxide interface towards enhanced low-temperature acetylene semi-hydrogenation, Nat. Commun. 12 (2021) 5770, https://doi.org/10.1038/s41467-021-25984-8.

[65] B. Lou, H. Kang, W. Yuan, L. Ma, W. Huang, Y. Wang, Z. Jiang, Y. Du, S. Zou, J. Fan, Highly selective acetylene semihydrogenation catalyst with an operation window exceeding 150 °C, ACS Catal. 11 (2021) 6073–6080, https://doi.org/10.1021/acscatal.1c00804.

[66] J. Zhang, W. Chen, H. Ge, C. Chen, W. Yan, Z. Gao, J. Gan, B. Zhang, X. Duan, Y. Qin, Synergistic effects in atomic-layer-deposited $PtCo_x$/CNTs catalysts enhancing hydrolytic dehydrogenation of ammonia borane, Appl. Catal. B Environ. 235 (2018) 256–263, https://doi.org/10.1016/j.apcatb.2018.04.070.